Combined effect of particle size and surface cohesiveness on powder spreadability for additive manufacturing

Yi He *, Ali Hassanpour, Andrew E. Bayly

School of Chemical and Process Engineering, University of Leeds, Leeds LS2 9JT, United Kingdom

ARTICLE INFO

ABSTRACT

The dependence of powder flowability on particle cohesion can often be captured by a dimensionless Bond number, however, whether the same is true for powder spreadability remains unclear. This paper thus presents a particle-scale study on the spreading of cohesive fine powders for additive manufacturing, focusing on the combined effect of particle size and surface cohesiveness. With an experimental validated model, detailed analysis revealed two competing mechanisms due to geometrical constraint and interparticle cohesion. For small particles that allows multiple particles across blade clearance, layer homogeneity is largely maintained before deteriorating sharply, while for large particles that forming a mono-layered packing structure, an optimum homogeneity can be obtained at a moderate level of particle cohesion. The efficacy of increasing blade clearance to improve layer quality was also evaluated. This study can help to identify a critical set of powder descriptors that defines spreading performance.

© 2021 The Authors. Published by Elsevier B.V. This is an open access article under the CC BY license (http://creativecommons.org/licenses/by/4.0/).

1. Introduction

Additive manufacturing (AM) has seen a rapid growth in many industrial sectors, transforming the production of parts with high geometrical complexity from rapid prototyping to industrial production, especially for safety-critical applications. For powder bed fusion (PBF) where a heat source is directly applied to consolidate powder materials, the quality of spread powder layer plays a key role in final fabricated parts through its influence on effective powder thermal conductivity, laser-material interaction and consequently dynamic of melt pool [1]. A dense and uniform powder layer are thus desired for both process optimization and control. However, feedstock materials are subject to considerable variability in particle properties, which can be induced during both atomisation processes and powder recycling [2], presenting a serious challenge for AM to manufacture parts of consistent and reliable quality. This is further complicated by the presence of a large number of influencing parameters, including both physical and chemical properties, and their interaction with the AM system, which drives the need for an in-depth understanding of the relationship between particle properties and powder spreadability.

Particle size is often regarded as a critical quality indicator for many powder-handling processes. For PBF processes, a smaller particle size is often preferred, as it permits a thin powder layer to be deposited and hence a better control of dimensional accuracy. However, due to the presence of attractive van der Waals interaction, decreasing particle

size results in an increase in particle cohesion, leading to reduced packing efficiency and flowability. Yang et al. [3] showed that packing density drops with decreasing particle size and open-tree structures can be observed on the surface of a packed bed. Meier et al. [4] observed a stiffer angle of repose and a reduced flowrate when discharging powders of a smaller particle size from hopper. A reduced powder flowability was also reported from measurements conducted by Brika et al. [5] on Ti-6Al-4V powder and by Balbaa et al. [6] on AlSi10Mg powder using both typical flowmeters and FT4 powder rheometer. However, as pointed out by Touzé et al. [7], standard flowability measurements still face difficulties to make a reliable estimation of powder spreadability. One reason for this is due to the fact that cohesive powders may not be able to flow through a typical Hall or Carney flowmeter, thus making it not possible to measure flow time or angle of repose of very cohesive powders. The stress condition in flowability tests also differs from that of shear-driven spreading, together with poor repeatability for cohesive powders, largely limiting their use to comparative testing.

From the viewpoint of processability, smaller particles require less heat for melting due to a smaller thermal inertia. Powder bed of fine particles also exhibits a higher specific surface area to volume ratio, which gives rise to an enhanced laser absorptivity. Balbaa et al. [6] observed 13% increase in laser absorptivity in terms of K-M absorption factor when d_{50} of AlSi10Mg powder decreases from 40 μm to 9 μm. Haeri et al. [8] showed that laser radiation pressure has a significant impact on powder dynamics, which affects particle trajectories at distances up to 1 cm and varies with particle size. Despite the preference for powders of a smaller particle size, a reduction of particle size does not guarantee

* Corresponding author.
E-mail addresses: y.he1@leeds.ac.uk (Y. He), a.e.bayly@leeds.ac.uk (A.E. Bayly).

a better part quality. For 316L stainless steel powder, Spierings et al. [9] showed that fine powder (with $d_{90} \sim 24\,\mu m$) results in a higher part density and mechanical strength than that of the coarser powder (with $d_{10} \sim 20\,\mu m$), which was attributed to a better packing efficiency seen by the fine powder. In contrast, Brika et al. [5] showed that a greater amount of fine particles in Ti-6Al-4V powder is detrimental to flowability and hence yields parts with reduced mechanical and geometric characteristics. Riener et al. [10] also reported a lower part density and a rougher part surface for AlSi10Mg powder with a higher amount of fine particles (with $d_{10} \sim 20\,\mu m$). Balbaa et al. [6] found that part fabricated by fine AlSi10Mg powder (with $d_{50} \sim 9\,\mu m$) has a lower quality in terms of density, surface roughness, dimensional accuracy, and microhardness than that of the coarser one (with $d_{50} \sim 40\,\mu m$). The reason was attributed to a poor flowability and agglomeration tendency observed by fine sized powder [6]. These studies further highlighted the importance of obtaining a high-quality powder layer, which stems the necessity to establish a quantitative correlation between particle size and powder spreadability.

However, knowledge on the role of particle size is still limited, partly due to the fact that particle-scale information is lacking from these experimental studies, making it difficult to conduct a quantitative evaluation on powder spreadability. Advanced experimental techniques, such as high-speed x-ray imaging [11], have made it possible to reveal in-situ spreading process but at present limited to the dynamics of powder pile in front of recoating blade. Ali et al. [1] combined nano-computing tomography with a UV curable polymer to bind particles, allowing an estimation of packing density at various locations in a spread powder bed. However, it still faces challenges to isolate the influence of particle size in feedstock. This is especially the case when considering interplay between particle size and other characteristics, such as surface cohesiveness and particle shape. For example, small particles with weak cohesiveness can fill the voids formed between large particles while, for strongly cohesive particles, the presence of fine particles would further hinder particle movement and deteriorate particle packing. In many powder-handling processes, the roles of particle size and surface cohesiveness can be captured by a lumped parameter (i.e., Bond number) defining the relative importance between interparticle cohesive force and particle gravity, which correlates well with packing density [12] and mixing index [13]. The same conclusion was also drawn for flow function coefficient obtaiend by shear cell tests [14] and for flowrate measured by vibration-asisted funnel discharging [7] which showed a good correlation with a population-dependent Bond number. Meier et al. [4] further confirmed from experiments and simulations that the effects of surface energy and particle size on the angle of repose formed by funnel discharging of Ti-6Al-4V powder can be well captured by the dimensionless Bond number. Despite the practical importance in powder spreading, experimental studies on how particle size and cohesiveness affect powder spreadability and whether it can be captured by the dimensionless Bond number remain limited.

The aforementioned limitations can be readily overcome by discrete element modelling (DEM) which provides abundant information at particle scale, allowing us to conduct controlled studies on the roles of particle properties and operational conditions in powder spreading [15–17]. For example, Haeri [18] proposed an optimized blade spreader with a super-elliptic head profile based on DEM simulations of spreading. The optimized blade spreader is capable of generating a powder bed comparable to that of roller spreader. Chen et al. [19] showed that both dynamic angle of repose and mass flowrate of particles being discharged from blade clearance are affected by particle size. An optimum powder flowability was found at a particle radius of 21.8 μm. Meier et al. [20] found that decreasing particle size is detrimental to layer quality, leading to lower and strongly varying packing density and highly irregular surfaces, which was also confirmed by Wang et al. [21] for the spreading of cohesive powders by a rotating roller. Ma et al. [22] studied the influence of volume fraction of fine powder (20 μm < d < 40 μm) on spreading. The layer quality was found to first

increase and then decrease with the amount of fine powder. Yao et al. [23] simulated the spreading of 316L stainless steel powder using DEM. A particle size of 30 μm is suggested to yield the optimum average packing density and structure uniformity. Recently, Shaheen et al. [24] highlighted the interplay between particle cohesiveness and process parameters, including spreading speed and spreading tool. Increasing spreading speed is detrimental for layer quality of non- and weakly cohesive powders but improves it for strongly cohesive ones [24]. Our recent study [25] showed that the presence of particle cohesion not only leads to features like patchy coverage, chain-like agglomerates and sparse particle distribution but also affects the dominating mechanism for spreading. Despite being success in qualitative understanding of spreading process, most of the previous DEM studies adopted a reduced particle stiffness that is several orders of magnitude smaller than the true physical value to speed up DEM simulations. However, the use of reduced particle stiffness results in an under-estimation of sliding and rolling resistances in the modelling of cohesive powders, consequently compromising the quantitative predictive capability of DEM modelling [26]. Moreover, despite individual influence of particle surface cohesiveness or particle size has been studied, the combined effect of particle size and surface cohesiveness on powder spreadability remains largely unresolved.

This study therefore conducts particle-scale simulations of powder spreading and systematically addresses the combined effect of particle size and surface cohesiveness on the quality of spread powder layer. Here, an efficient simulation is made possible by leveraging GPU computing. Moreover, a stiffness scaling methodology [26] is adopted to handle the use of reduced particle stiffness in modelling cohesive particles, enabling us to establish a quantitative prediction of the quality of spread powder layer. The characteristics of deposited powder layer is assessed in terms of packing density, coordination number and surface profile. The rest of the paper is structured as follows: numerical methodology is first outlined in Section 2, followed by a brief description of simulation conditions and analysis techniques in Section 3. A preliminary test on model performance is presented in Section 4, where comparisons with experimental results in literature were made on static angle of repose (AOR) formed by powders of different particle size distributions. It should be noted that quantitative validation on the quality of spread powder bed is not aimed here, instead the focus is given to the combined effects of particle size and surface cohesiveness on the quality of spread powder layer in section 5, together with evaluation on the efficacy of increasing blade clearance to improve layer quality. The conclusions and outlook are presented in section 6.

2. Model description

In DEM, the motion of individual particles is updated according to Newton's second law of motion. The soft-sphere model is adopted, which is capable of explicitly incorporating material properties and interaction laws between two particles. The translational and rotational motions for a particle of mass m_i and moment of inertia I_i are governed by,

$$m_i \frac{d\mathbf{v}_i}{dt} = \sum_j \left(\mathbf{F}_{cn,ij} + \mathbf{F}_{dn,ij} + \mathbf{F}_{ct,ij} + \mathbf{F}_{dt,ij} \right) + \sum_k \mathbf{F}_{v,ik} + m_i \mathbf{g} \quad (1)$$

$$I_i \frac{d\boldsymbol{\omega}_i}{dt} = \sum_j (\mathbf{T}_t + \mathbf{T}_r) \quad (2)$$

where $\mathbf{v}_i$ and $\boldsymbol{\omega}_i$ are the translational and rotational velocities, respectively. The forces acting on particle i by particle j consist of contact forces ($\mathbf{F}_{cn,ij}$ and $\mathbf{F}_{ct,ij}$) and damping forces ($\mathbf{F}_{dn,ij}$ and $\mathbf{F}_{dt,ij}$) in both normal and tangential directions. $\mathbf{F}_{v,ik}$ represents van der Waals force imposed on particle i by particle k, which is known to be important for fine particles.

The normal contact force ($\mathbf{F}_{cn,ij}$) was calculated according to the Hertzian model [27], given by,

$$\mathbf{F}_{cn,ij} = \frac{4}{3} E^* R^{*1/2} \delta_n^{3/2} \widehat{\mathbf{n}} \tag{3}$$

where $E^* = E_i E_j/(E_i + E_j)$ is the effective elastic modulus with $E_i = Y_i/(1 + \nu_i^2)$. Y is particle Young's modulus and ν is Poisson's ratio. $R^* = R_i R_j/(R_i + R_j)$ is the effective particle radius. $\mathbf{F}_{dn,ij}$ is the normal damping force responsible for energy dissipation due to inelastic collisions, given by,

$$\mathbf{F}_{dn,ij} = 2\sqrt{\frac{5}{6}} \beta_n \sqrt{S_n m^*} \mathbf{v}_{ij}^n \tag{4}$$

in which β_n is the normal damping coefficient. $m^* = m_i m_j/(m_i + m_j)$ is the effective mass and $S_n = 2E^*\sqrt{R^*\delta_n}$.

The van der Waals force ($\mathbf{F}_{v,ik}$) is calculated based on the Hamaker theory [28], given by,

$$\mathbf{F}_{v,ik} = \begin{cases} \dfrac{AR^*}{6s_{min}^2} \widehat{\mathbf{n}} & s < s_{min} \\[2mm] \dfrac{AR^*}{6s^2} \widehat{\mathbf{n}} & s_{min} \leq s \leq s_{max} \\[2mm] 0 & s \geq s_{max} \end{cases} \tag{5}$$

where $s = |\mathbf{r}_i - \mathbf{r}_k| - (R_i + R_k)$ is the interparticle separation distance. A is Hamaker constant, which depends on both physical and chemical properties of particle, such as surface roughness, medium chemistry, and temperature. s_{min} is a cut-off distance introduced to avoid the singularity when the surface separation equals to zero, below which van der Waals force is assumed to be constant. A maximum cut-off distance s_{max} is also introduced to limit calculation expenses, due to the fact that the magnitude of van der Waals force drops shapely with increasing interparticle separation.

The Hamaker theory is adopted here mainly due to its simplicity, which assumes a constant cohesive force when two particles are in contact. In contrast, the JKR theory [29] is more suitable for soft materials with a large surface energy. The applicability of JKR theory can be characterised by the Tabor parameter defined as $T_a = (4R\gamma^2/E^2 s_{min})^{1/3}$, with γ the surface energy [30]. The JKR theory generally applies for $T_a > 3.0$ while T_a is in the order of 10^{-9} for the metallic powders considered in this study. Moreover, Roy et al. [31] showed that the functional form of non-contact cohesive model has little impact on bulk behaviour, as long as the maximum adhesive force and total energy dissipation per contact are matched. In fact, based on the JKR theory, the value of Hamaker constant can be related to surface energy by the following equation [32],

$$\gamma = \frac{A}{24\pi s_{min}^2} \tag{6}$$

In the tangential direction, $\mathbf{F}_{ct,ij}$ and $\mathbf{F}_{dt,ij}$ are the frictional contact force and the damping force, given as [27].

$$\mathbf{F}_{ct,ij} = \begin{cases} -\mu_t |\mathbf{F}_{cn,ij}| \left[1 - (1 - |\boldsymbol{\delta}_t|/\delta_{t,max})^{3/2} \right] \widehat{\boldsymbol{\delta}}_t & |\boldsymbol{\delta}_t| < \delta_{t,max} \\[2mm] -\mu_t |\mathbf{F}_{cn,ij}| \widehat{\mathbf{v}}_t & |\boldsymbol{\delta}_t| \geq \delta_{t,max} \end{cases} \tag{7}$$

$$\mathbf{F}_{dt,ij} = 2\sqrt{\frac{5}{6}} \beta_t \sqrt{S_t m^*} \mathbf{v}_{ij}^t \tag{8}$$

where μ_t is the coulomb friction coefficient. $\boldsymbol{\delta}_t$ is the particle displacement in the tangential direction and $\widehat{\boldsymbol{\delta}}_t = \boldsymbol{\delta}_t/|\boldsymbol{\delta}_t|$. $\widehat{\mathbf{v}}_t = \mathbf{v}_t/|\mathbf{v}_t|$ is the unit vector of the relative velocity in the tangential direction. $\delta_{t,max} = \mu_t \delta_n (2 - \nu)/(2 - 2\nu)$ and β_t is the tangential damping coefficient. $S_t = 8G^*\sqrt{R^*\delta_n}$, where $G^* = G_i G_j/(G_i + G_j)$ the effective shear modulus, with $G_i = Y_i/2(2 - \nu_i)(1 + \nu_i)$. The torques acting on the particle consists of a torque due to the tangential forces $\mathbf{T}_t = \mathbf{R}_i \times \mathbf{F}_{t,ij}$ and a rolling resistance torque due to the asymmetric distribution of the contact pressure $\mathbf{T}_r = \mu_r |\mathbf{F}_{cn,ij}| \boldsymbol{\omega}_i/|\boldsymbol{\omega}_i|$, where μ_r is the rolling friction coefficient.

A reduced particle stiffness that is several orders of magnitude lower than the true physical value is often adopted to speedup DEM simulations, as the maximum allowable DEM timestep is related to both particle size and stiffness. However, a reduced particle stiffness leads to an over-dissipated kinetic energy by cohesive interaction, the cohesive force thus needs to be scaled to preserve the original particle behaviour. In this work, a recently developed stiffness scaling methodology is adopted, which extends the applicability of using reduced particle stiffness to contact-dominated systems [26]. It consists of three key components. For contact adhesion, a reduced Hamaker constant is calculated based on the scaling ratio of Young's modulus, given by,

$$A^R = A^O \left(Y^R/Y^O \right)^{2/5} \tag{9}$$

where the superscripts R refers to reduced particle properties while O refers to the original particle properties. In the calculations of sliding and rolling resistances, a modified normal contact force ($\mathbf{F}_{cn,ij}^M$) is introduced, given by,

$$\left| \mathbf{F}_{cn,ij}^M \right| = \left| \mathbf{F}_{cn,ij} \right| - \left| \mathbf{F}_{v,ij} \right| + \left| \mathbf{F}_{v,ij}^O \right| \tag{10}$$

where $|\mathbf{F}_{cn,ij}|$ and $|\mathbf{F}_{v,ij}|$ are calculated using the reduced particle stiffness. As the van der Waals force during contact is assumed constant, $|\mathbf{F}_{v,ij}^O|$ can be calculated directly using the original Hamaker constant A^O. To account for enlarged DEM time step and discontinuity of van der Waals force introduced by reduced particle stiffness, an impulse-based force estimation scheme is introduced, given by,

$$\mathbf{F}_{v,i} = \sum_k \frac{m_i(v_{i,n} - v_{i0,n}) \widehat{\mathbf{n}}_{ik}}{\Delta t_{DEM}} \tag{11}$$

The summation runs over all neighbouring particles of particle i. Δt_{DEM} is the enlarged DEM timestep. $v_{i0,n}$ is the particle velocity without considering non-contact van der Waals interaction while $v_{i,n}$ is the corrected particle velocity which can be calculated by enforcing momentum and energy conservations between two interacting particles. More details of the calculation can be found in the previous study [26]. It has been shown that, with this new stiffness scaling methodology, the properties of both packed bed and spread powder bed of cohesive powders can be well preserved when the particle stiffness is scaled down to four orders of magnitude.

3. Simulation condition and data analysis

The modelled system mimics a generic powder spreading configuration, comprising a rigid recoating blade and a rough rectangular substrate with a dimension of $40d_p \times 600d_p$, where d_p is the particle diameter. Fig. 1 shows schematically the modelling configuration, similar to that used in the previous study [25]. Periodic boundary condition is applied to the front and rear sides of the computational space to eliminate wall effects. The rigid blade has a width same as the base in the Y direction, i.e., $40d_p$, and a thickness of 200 μm. A packed bed is first generated by random generation of mono-sized spherical particles without overlap within a confined space formed by placing a rigid vertical gate $40d_p$ in front of the blade, as shown in Fig. 1(a). The vertical gate is then removed, allowing a stable heap to be formed in front of the blade under the effect of gravity (Fig. 1(b)). Finally, the blade is lifted to form a constant vertical gap of 100 μm between the blade and substrate for spreading (Fig. 1(c)). For all the cases, a constant spreading speed of 50 mm/s is specified in the X direction and a total length of $500d_p$ is spread. The first $100d_p$ of a spread powder bed and $10d_p$ immediately behind the spreading blade are excluded from data analysis. Data sampling is conducted within a length of $390d_p$, as shown in
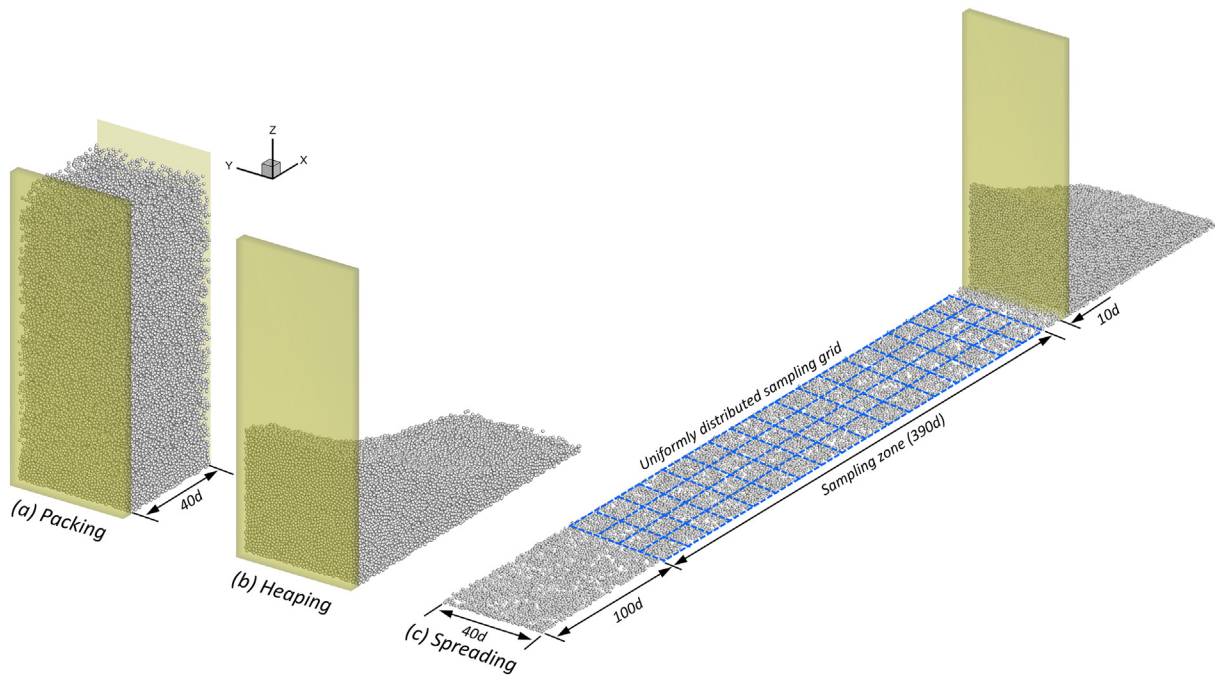
Fig. 1. Schematics of the modelling configuration and sampling zone of spread powder bed.

Fig. 1(c). As shown in Fig. 1(c), a Cartesian 2D sampling grid is used to aid the sampling of local properties according to a recently developed digital-based characterisation approach [33].

Table 1 summarise the parameters used for the simulations, in which particle properties are typical of a Ti-6Al-4V powder, similar to that used by Meier et al. [20]. A minimum cut-off distance s_{min} is introduced for the calculation of van der Waals interactions [32]. The material properties of wall are the same as that of particles but with an infinitely large contact radius when handling particle-wall interactions.

To accelerate calculation, an in-house GPU-based DEM code (HiPPS) is used for all simulations. The stiffness scaling methodology allows particle stiffness to be safely reduced by three orders of magnitude for cohesive fine particles, resulting in an enlarged DEM time step which is 31.6 times of that of the original particle stiffness. Particle size and suface cohesiveness are systematically varied to explore their combined influence on the quality of spread powder layer while keeping other parameters constant. According to the JRK theory, the tested value of Hamaker constant corresponds to an effective surface energy ranging from 0 to 3.62 mJ/m². Particle surface cohesiveness can be varied by different reasons, for example, changes of chemical (i.e., surface chemistry,

and potential contamination and oxidization) and geometrical properties (due to surface asperities) of particles. The Hamaker constant is defined relative to a base value of a_1 (i.e., 3.72×10^{-23}) which leads to a Bond number (*Bo*) of 1.0 for particles of size 50 μm, where *Bo* is defined as the ratio of the maximum pull-off force to particle gravity. For van der Waals interaction, *Bo* can be calculated as,

$$Bo = \frac{F_{v,max}}{mg} = \frac{A}{16\pi R^2 \rho g s_{min}^2} \qquad (12)$$

4. Model validation

To gain confidence on the simulation results, a preliminary test on model performance is conducted by comparing with literature results on the static angle of repose formed by Ti-6Al-4V powder samples in heaping. The modelling set-up is shown schematically in Fig. 2(a), where a vibrating funnel is used to facilitate the discharge of cohesive powders. Three different particle size distributions are examined here, denoted as fine, medium and coarse powders, as shown in Fig. 2(b), consistent with that used in the experiments of Meier et al. [4]. The effective surface energy is first calibrated by matching AOR from modelling with that measured on the medium-sized powder, where the AOR is calculated by fitting a triangle onto a 2D projection of the heap, as shown in Fig. 2(a). The calibrated effective surface energy is then used to predict AORs of the coarse and fine samples, respectively. Comparisons of predicted AORs with that measured in experiments are made so that model performance can be evaluated.

Fig. 3(a) shows the numerical AOR as a function of effective surface energy, with other parameters kept the same as that listed in Table 1. A surface energy of 0.142 mJ/m² is calibrated by linear interpolation, corresponding to a Hamaker constant of 2.91×10^{-22} J (i.e., $A = 7.84a_1$). It is slightly larger than that calibrated by Meier et al. [4] (i.e., 0.1 mJ/m²). The discrepancy can be attributed to the difference in contact force model and the consideration of stiffness scaling in the present study. It is worthy to note that the calibrated effective surface energy is also significantly smaller than that measured for flat metal contact surfaces, because of the difference in surface properties.

Table 1
Parameters used in the present simulations.

| Parameter	Value
Particle number, N_p	100,000
Particle diameter, d_p(μm)	25, 30, 40, 50, 60, 75, 90, 100
Density, ρ(kg/m³)	4430
Original Young's modulus, Y^O(GPa)	110
Reduced Young's modulus, Y^R(GPa)	0.11
Poisson ratio, ν	0.3
Sliding friction coefficient, μ_t	0.3
Rolling friction coefficient, μ_r	0.01
Restitution coefficient, e	0.4
Hamaker constant, a_1(J)	3.72×10^{-23}
Minimum cut-off distance, s_{min}(m)	1.65×10^{-10}
Blade gap, δ_b(μm)	100
Blade thickness, t_b(μm)	200
Blade speed, v_b(mm/s)	50
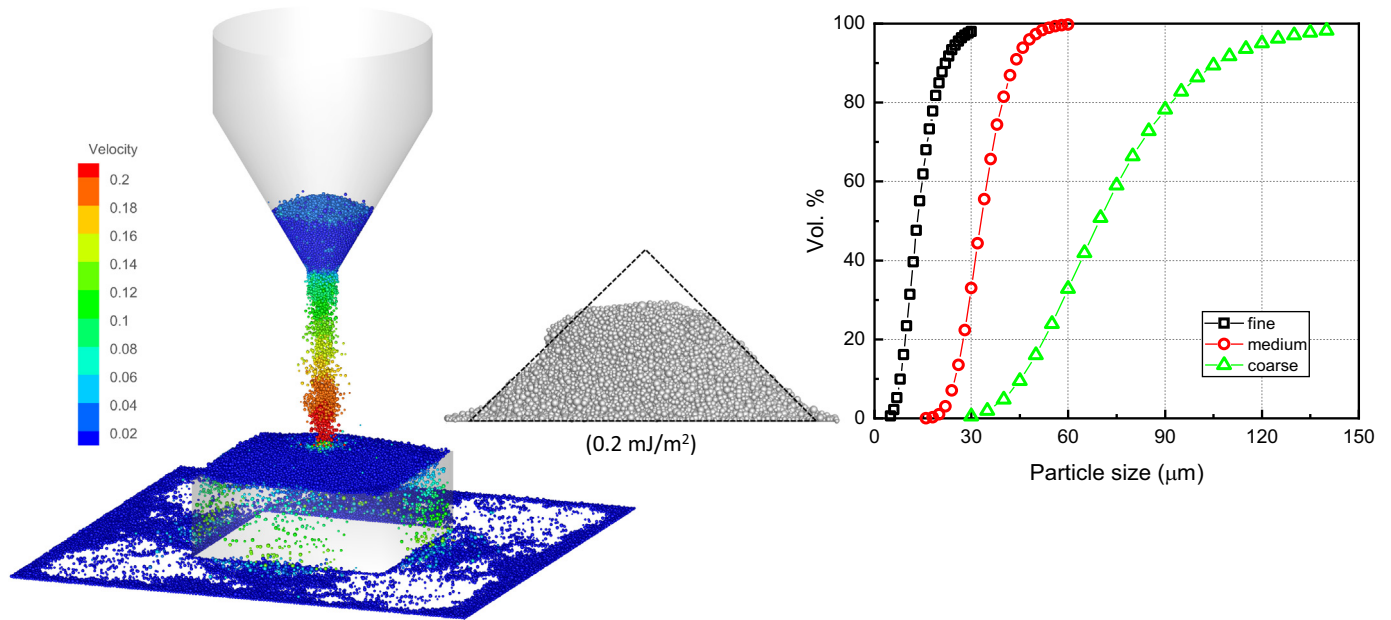
Fig. 2. Schematic of the heaping simulation and volume-based cumulative particle size distributions of powder samples, following that used in the experiments of Meier et al. [4].

With the calibrated surface energy, the predicted AORs of powders of different particle size distributions agree well with that measured experimentally, which confirms the validity of DEM model in predicting heaping behaviour of Ti-6Al-4V powder. However, it is worthwhile to note that static AOR is not a good metric for model calibration and validation of cohesive fine powders, although it is used here as a compromise due to the lack of particle-scale information on a spread powder layer. The reason is mainly related to the irregularity of slope surface observed for highly cohesive powders, as shown in Fig. 2(a), making it difficult to obtain an accurate estimation of AOR. Furthermore, AOR is insensitive to the change of surface energy for highly cohesive powders, as shown in Fig. 3(a).

Further studies are thus required to enable a more accurate calibration of effective surface energy for powder spreading. However, it should be emphasized that, although the stress condition in heaping is different from the dynamic spreading at high strain rate, the force model and stiffness scaling methodology used here has been verified in the previous studies [25,26], showing the capability of achieving quantitative predictions using DEM. Since the present study is focused on the fundamental understanding of the combined effect of particle size and surface cohesiveness, the validation test presented here provides not only further confidence in the model but also a basis for the selection of tested range of surface cohesiveness in the following parametric study.

5. Results and discussion

5.1. Packing structure

Fig. 4 shows the top view of spread powder layers formed by different combinations of particle size and surface cohesiveness, in which particles are coloured by coordination number (*CN*), i.e., the number of particles in contact with a given particle. A cut-off distance of $1.005d_p$ was introduced to determine whether two particles are in contact. Since there is no clear structural variation in the spreading direction, only a small section of the spread powder layer is shown here, with a dimension of $40d_p \times 100d_p$.
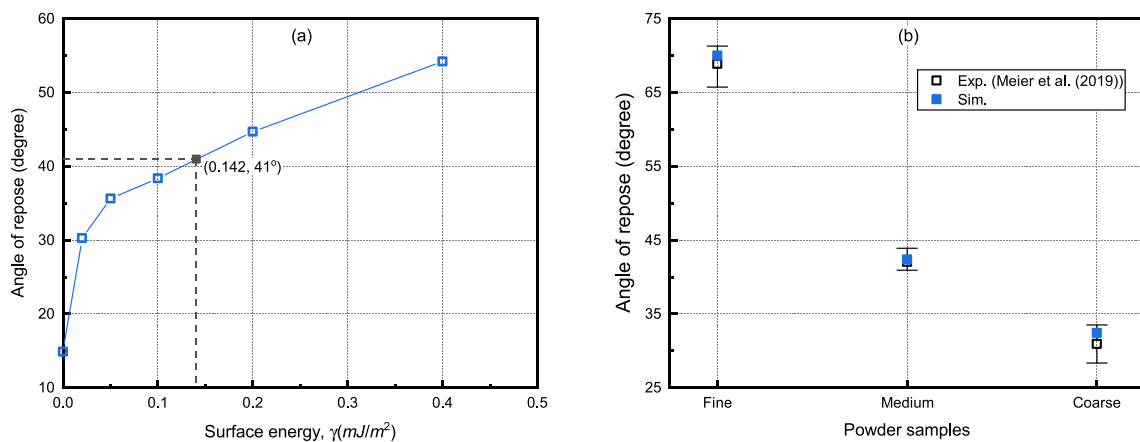

Fig. 3. (a) Calibration of surface energy and (b) model validation in predicting AORs of powders of different particle size distribution. Comparisons are made against experimental results reported by Meier et al. [4].
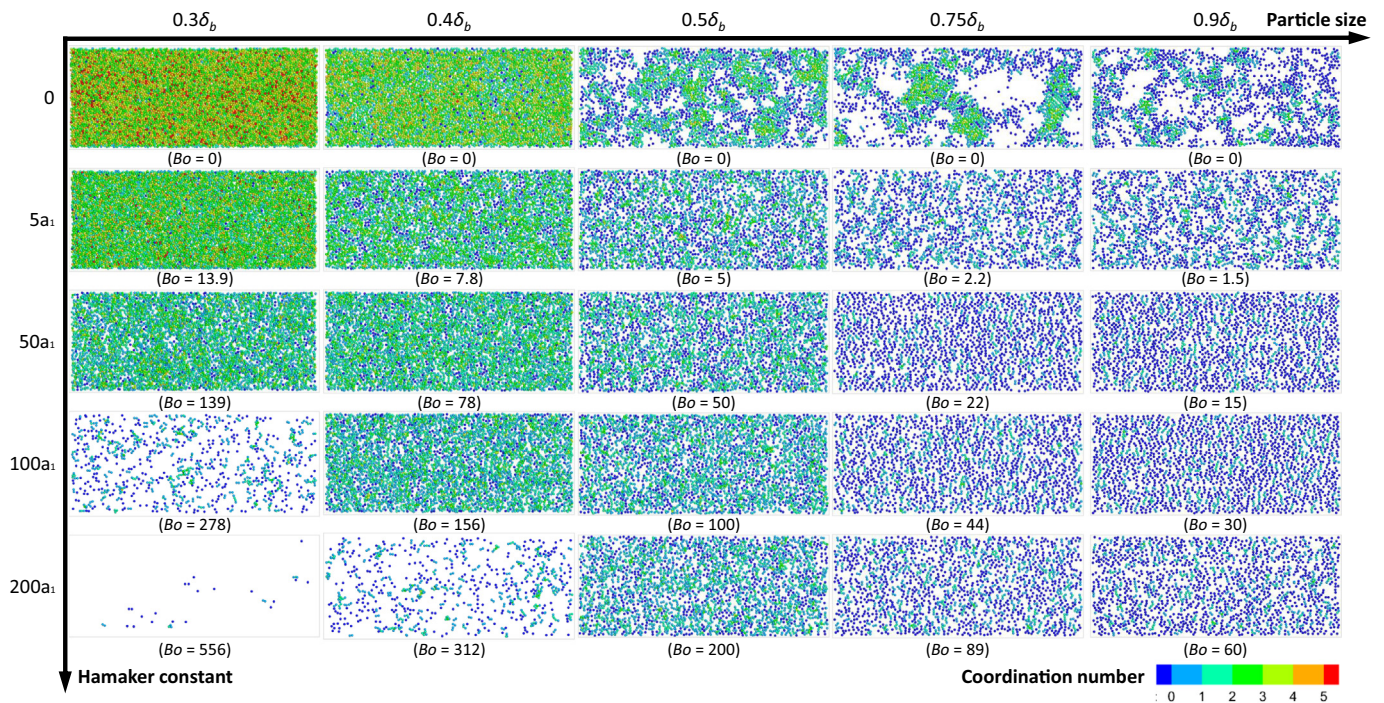
Fig. 4. Top view of spread powder bed of different combinations of particle size and effective Hamaker constant. Only a section of the spread bed is shown here, with a dimension of $40d_p \times 100d_p$.

It can be seen from Fig. 4 that the effects of particle size and surface cohesiveness are closely correlated. For particles of small surface cohesiveness (i.e., $A \leq 5a_1$), a continuous and densely packed layer is observed for small particles (i.e., $d_p \leq 0.5\delta_b$) while defects, such as empty patches or voids, start to emerge with increasing particle size. The layer structure is thus mainly determined by the geometrical constrain created by a given blade clearance. A smaller particle size means more particles can be discharged through the blade, consequently leading to a multiple-layered, uniform, and densely packed structure. In contrast, mono-layered, non-uniform structure dominants the spread powder

layer of large particles (i.e., $d_p > 0.5\delta_b$). The majority of particles have a CN smaller than 4, with an appreciable ratio of free particles (i.e., no contact with other particles). The formation of large empty patches can be attributed to collision-induced particle clustering as particle gain a large momentum to continue moving forward [25]. The distance travelled by cohesive particles is much shorter than that of non-cohesive particles due to particle-substrate adhesion. Consequently, compared to cohesive particles, non-cohesive particles have a higher chance to collide with each other, forming larger empty patches. As an example, Fig. 5 shows the velocity distributions for particles of size
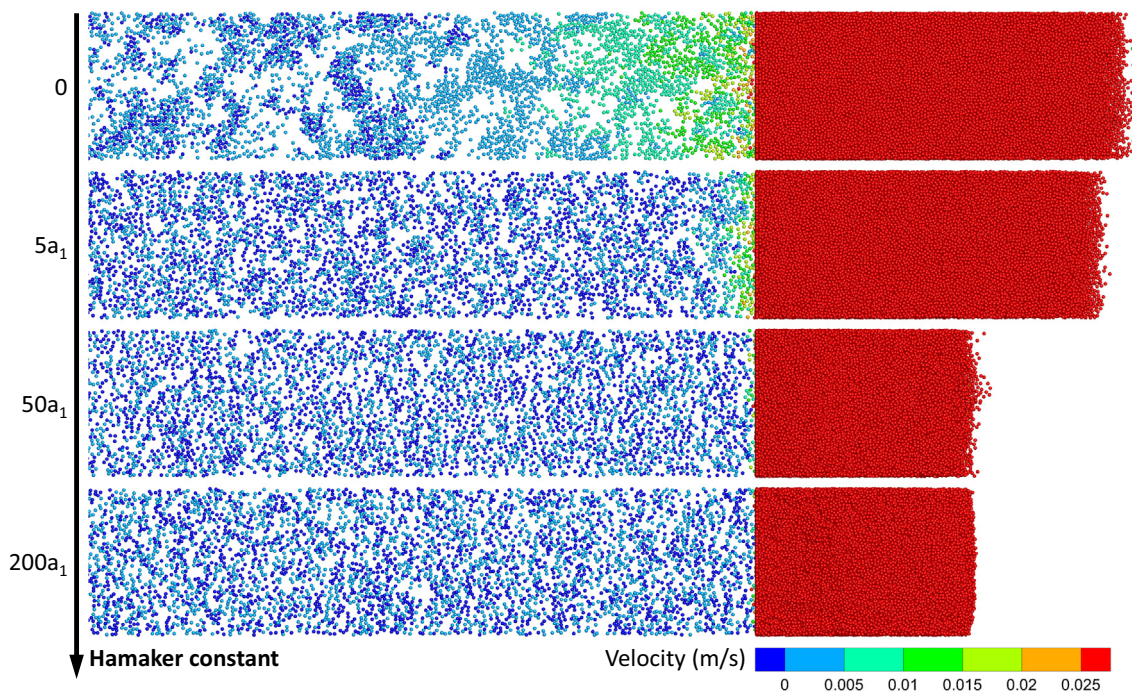

Fig. 5. Velocity distribution for particles of size $0.6\delta_b$ during spreading, where particles are coloured by velocity in the spreading direction.

$0.6\delta_b$, where residual momentum of particles after being discharged from the blade decreases with increasing surface cohesiveness. Particles are distributed more uniformly immediately behind the blade than that further away from it, which is especially the case for non-cohesive and weakly cohesive powders. For strongly cohesive powder, the uniformity of both spatial distribution and velocity distribution is largely maintained after being discharged.

For particles of a moderate surface cohesiveness (i.e., $A = 50a_1$), particles of a smaller size still yield a more densely packed layer than that of the larger particles while layer homogeneity appears to be less sensitive to the variation of particle size. However, when $A > 50a_1$, particle cohesion takes over as the dominant mechanism affecting the layer structure. A sparse and non-uniform structure is observed for powders of a small particle size and chain-like agglomerates can be observed when particle size is larger than $0.5\delta_b$, largely attributed to the presence of strong interparticle attractive forces. The homogeneity of spread powder layer increases with particle size, as the magnitude of interparticle cohesive force decreases with increasing particle size.

Fig. 6(a) shows the effect of particle size on the frequency distribution of CN in spread layers for different Hamaker constants. For particles with a small surface cohesiveness (i.e., $A \le 5a_1$), CN of small particles (i.e., $d_p \le 0.5\delta_b$) varies from 0 to 8, largely following a Gaussian distribution. With increasing particle size, the distribution gradually shifts towards left and get truncated at the lower side, primarily due to a stronger wall effect. However, CN shows little variation with particle size when it is larger than $0.5\delta_b$. In contrast, for particles with strong surface cohesiveness (i.e., $A \ge 50a_1$), CN decays almost exponentially for large particles. There is little difference in CN among small particles (i.e., $d_p \le 0.5\delta_b$) whereas an increase in the ratio of free particles (i.e., $CN = 0$) is seen with increasing particle size for particles larger than $0.5\delta_b$. The resulting packing structure is thus mainly governed by surface cohesiveness for large particles (i.e., $d_p > 0.5\delta_b$) with weak cohesiveness and small particles (i.e., $d_p \le 0.5\delta_b$) with strong cohesiveness. The same data is replotted in Fig. 6(b) to highlight the role of surface cohesiveness. For small particles (i.e., $d_p < 0.5\delta_b$), the distribution shifts

towards left with increasing Hamaker constant, showing a decreased mean value. This corresponds to a structural transition from a multiple-layered to a single-layered packing structure. It is worthwhile to note that the spread of distribution is less sensitive to the change of Hamaker constant up to a value of $50a_1$. The same is also true for large particles, where CN follows an exponential decay for all the Hamaker constants tested. The increase of Hamaker constant leads to a slightly increase in the ratio of small CN (i.e., $CN \le 1$), indicating an enhanced homogeneity of particles dispersed over the base substrate.

The packing structure of spread powder layer can be further revealed from frequency distribution of particle coordinates in the vertical direction. As shown in Fig. 7, the first peak at $0.5d_p$ represents the layer of particles deposited on the substrate. Multiple layers can be seen by particles smaller than $0.5\delta_b$. Specifically, for particle size of $0.3\delta_b$, there is a well-defined second peak around $1.3d_p$ for non-cohesive particles, which corresponds to the presence of a close packed periodicity as observed previously [17]. With increasing surface cohesiveness, the distribution at the second peak becomes more dispersed and the peak is less defined, suggesting a shift towards a disordered packing. The maximum height of particles is seen to increase with surface cohesiveness, reaching a maximum value of $2.9d_p$ when Hamaker constant is larger than $50a_1$. However, the maximum layer thickness is bound by the blade clearance, same for other particle sizes tested here. For particles of size $0.4\delta_b$, nearly 90% of non-cohesive particles are found in the first layer. The increase of surface cohesiveness first increases the ratio of particles located off the substrate without much effect on the position of the second peak around $1.2d_p$. However, a further increase to $50a_1$ leads to a right shift of the second peak and a third peak around $2.0d_p$ starts to emerge, due to an increased level of particle agglomeration. In contrast, spread layers formed by particles larger than $0.5\delta_b$ are dominated by mono-layered packing structure, although only the case of $0.75\delta_b$ is shown here for brevity. Increasing surface cohesiveness only slightly decreases the ratio of particles touching the substrate, mainly due to the geometrical constrain of the blade clearance.
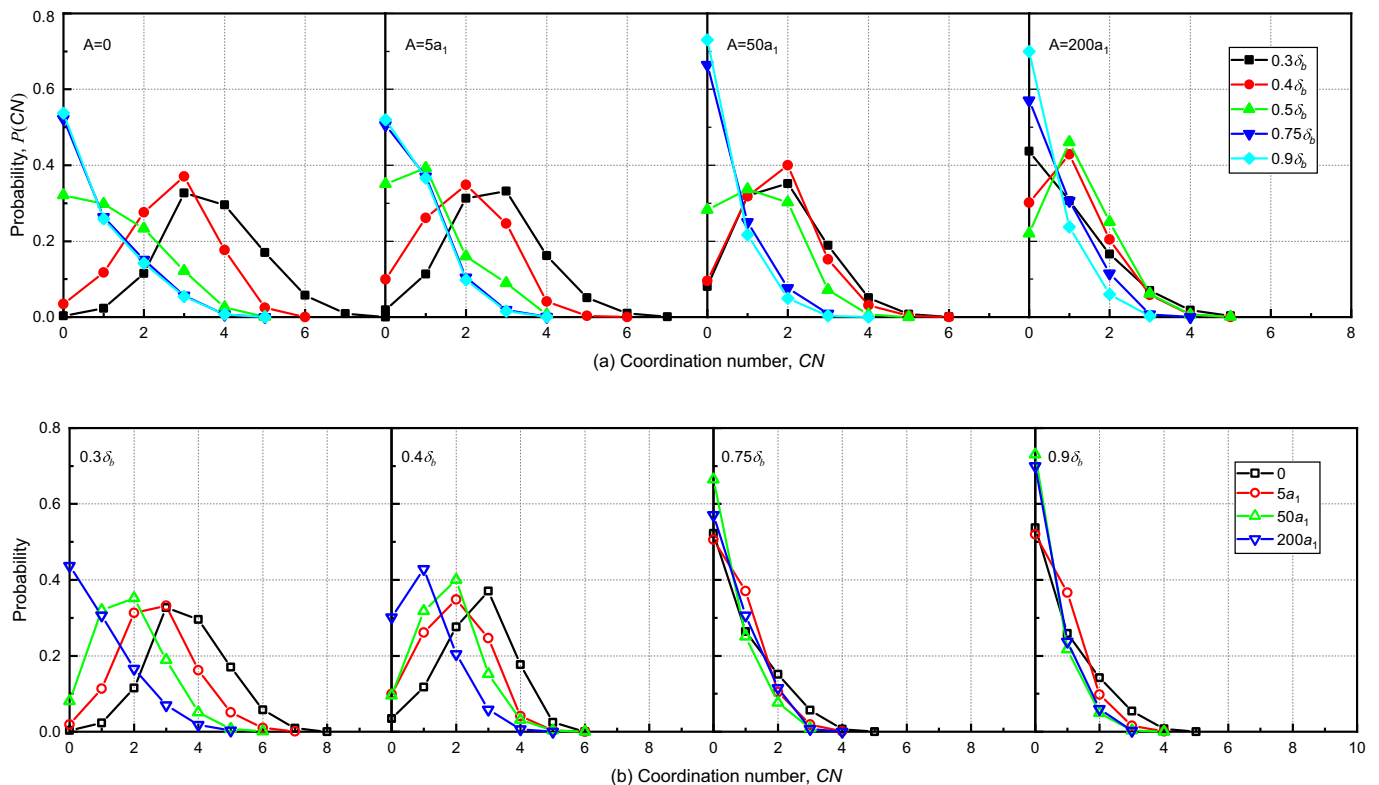

Fig. 6. Distribution of coordination number for particles of different sizes and particle cohesiveness.
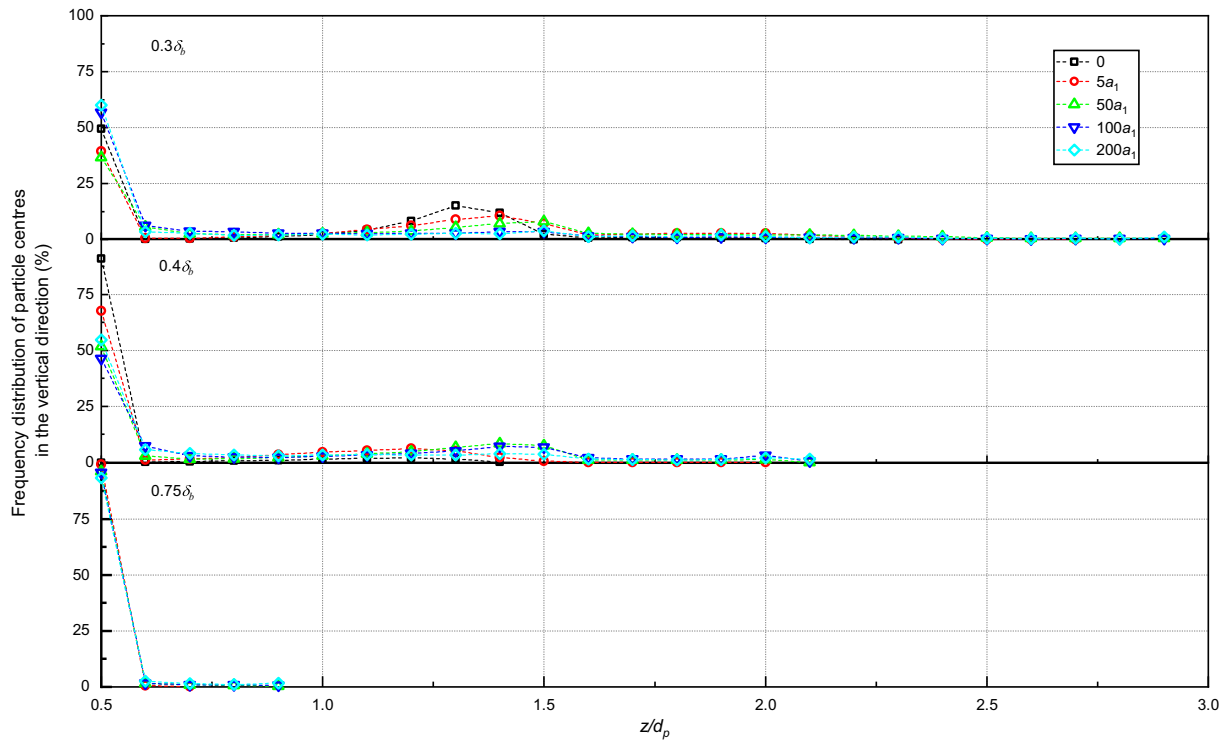
Fig. 7. Vertical distribution of particle centres within spread layers of different Hamaker constants.

5.2. Packing density

By sampling local packing density using a 2D grid, spatial distribution of packing density can be revealed, based on which layer uniformity can be evaluated. Fig. 8 shows the spatial distributions of packing density, with the same sampling parameters used among different cases.

Overall, small particles with strong surface cohesiveness and large particles with weak surface cohesiveness are detrimental to layer quality, where localized regions of large packing density can be observed across the spread layer. For large particles (i.e., $d_p > 0.5\delta_b$), the confined space due to blade clearance only allows a single layer of particles to be deposited. The discontinuities of density distribution observed with smaller
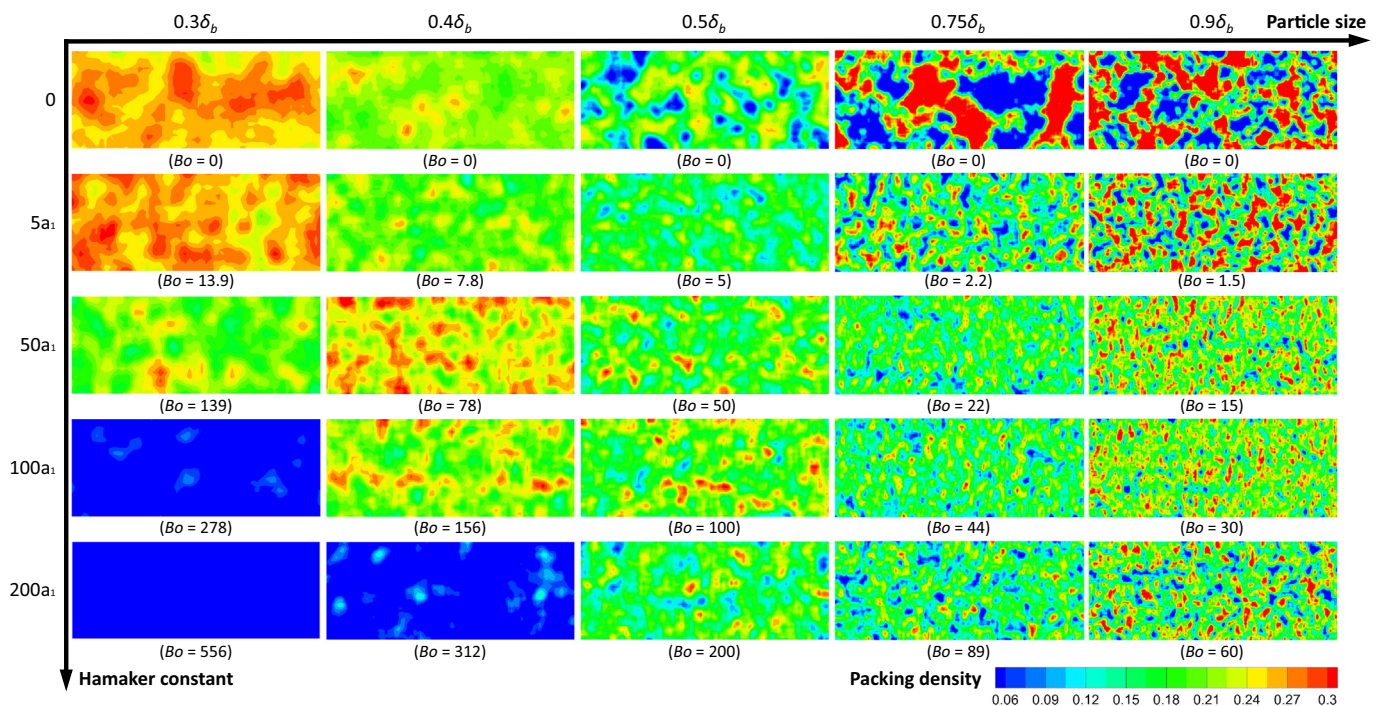

Fig. 8. Distribution of local packing density of spread powder layer affected by both particle size and effective Hamaker constant. Only a section of the spread bed is shown here, with a dimension of $40d_p \times 100d_p$.

Hamaker constants are thus likely to be caused by collision-induced particle clustering, as particles gained a large momentum to continue moving forward. However, with increasing Hamaker constant, these localized high-density regions not only reduce in size but also distribute more uniformly across the bed, which can be attributed to two possible reasons. Firstly, the increase of interparticle cohesive force facilitates the form of chain-like agglomerates, causing elongated shape of these high-density regions. Secondly, the residual momentum of particles after being discharged is quickly dissipated due to an enhanced particle-wall adhesion, thus leading to a homogeneous distribution of these high-density regions. In general, the smaller the particle size, the more particles that can be discharged from the blade gap. This does not only lead to a significant decrease of mean free length that a particle can travel before colliding with other particles. For particles of small surface cohesiveness (i.e., $A < 5a_1$), the momentum particle gained from discharging also enables it to rearrange within the deposited layer. Consequently, small particles demonstrate a higher average packing density and a better uniformity than that of the large particles. However, for particles of a large surface cohesiveness (i.e., $A \geq 50a_1$), decreasing particle size leads to an increase and followed by a decrease in both average packing density and layer homogeneity. This is likely to be caused by two competing effects. On the one hand, small particle size allows more than one layer of particles to be deposited, which can improve the layer quality due to a reduced wall effect. On the other hand, interparticle cohesive force increases considerably with decreasing particle size compared to particle gravity (i.e., a large Bo), thus hindering particles from being discharged from the gap and consequently leading to a poor layer quality.

Fig. 9(a) shows the effect of particle size on median packing density of spread layers for different Hamaker constants. For large particles, the median packing density of different Hamaker constants largely follows a similar trend, decreasing almost linearly with the decrease of particle size. However, different trends are observed for smaller particles (i.e., $d_p \leq 0.5\delta_b$). With decreasing particle size, a linear increase in the median packing density is observed for particles with small Hamaker constants while a sharp drop is seen after an initial increase for $A \geq 50a_1$. This discrepancy can be related to the strong van der Waals force which hinders particles to be discharged. In Fig. 9(b), the homogeneity of density distribution is quantified by the ratio of interquartile range (IQR) to median packing density, which is more robust than coefficient of variation to the presence of outliers. A large IQR\Median ratio means a high level of density dispersion. With decreasing particle size, the IQR\Median ratio decreases slightly for large particles (i.e., $d_p > 0.5\delta_b$) with small Hamaker constants (i.e., $A < 50a_1$) but remains almost constant for that of larger Hamaker constants (i.e., $A \geq 50a_1$). When particles are smaller

than $0.5\delta_b$, the IQR\Median ratio continues to decrease for particles with small Hamaker constants. In particular, the IQR\Median ratio remains very low when particle size is smaller than $0.4\delta_b$, suggesting an optimal layer quality can be obtained by small particles with weak surface cohesiveness. However, the IQR\Median ratio increases considerably with decreasing particle size for large Hamaker constants. Therefore, decreasing particle size is detrimental to layer quality for particles with strong surface cohesiveness, which results in a sparse and inhomogeneous particle distribution as shown in Fig. 4.

The median packing density is plotted in Fig. 10 as a function of Bond number. As shown in Fig. 10(a), for small particle sizes (i.e., $d_p \leq 0.5\delta_b$), there is a limiting Bo around 100 which differentiate the dependence of median packing density on Bo. The median packing density remains largely constant for $Bo < 100$ while it drops exponentially with Bo when $Bo > 100$. For particles larger than $0.5\delta_b$, as shown in Fig. 10(b), the median packing density shows little dependence on Bo, except a slightly decrease of the median packing density observed at large Bo. It can be seen that the median packing density can be expressed as a function of d_p/δ_b and Bo, where the adhesion effect takes over geometrical effect as the dominant factor affecting particle deposition in spreading when $Bo > 100$.

Fig. 11 plots the IQR/Median ratio as a function of Bond number. Similar to that of median packing density, the IQR/Median ratio of small particles (i.e., $d_p \leq 0.5\delta_b$) remain relatively low and stable for $Bo < 100$ while further increase of Bo leads to an exponential increase in the ratio, suggesting a significant deteriorated layer homogeneity. On the other hand, for large particles (i.e., $d_p > 0.5\delta_b$), an optimum layer homogeneity can be obtained at a moderate Bo between 10 and 100, especially so for that of a large d_p/δ_b ratio.

5.3. Surface profile

Fig. 12 shows the surface profile sampled from spread layers of different particle sizes and Hamaker constants. The surface profile is sampled with the aid of a 2D Cartesian grid. At each grid node, sampling is conducted within a domain of a square base with a size of 20 μm. Local surface height is determined as the maximum vertical coordinate of solid voxel found within the local sampling domain. More details of the characterisation approach can be found in our previous work [33]. As multiple layered packing structure is allowed for small particles (i.e., $d_p \leq 0.5\delta_b$), the initial increase of surface cohesiveness facilitates particle agglomeration on the bed surface due to the presence of van der Waals interaction, consequently leading to an increase in the ratio of higher surfaces. Further increase of Hamaker constant, however, hinders particle deposition, leading to the formation of voids and thus an increase in the ratio of lower surfaces. In general, non-cohesive particles
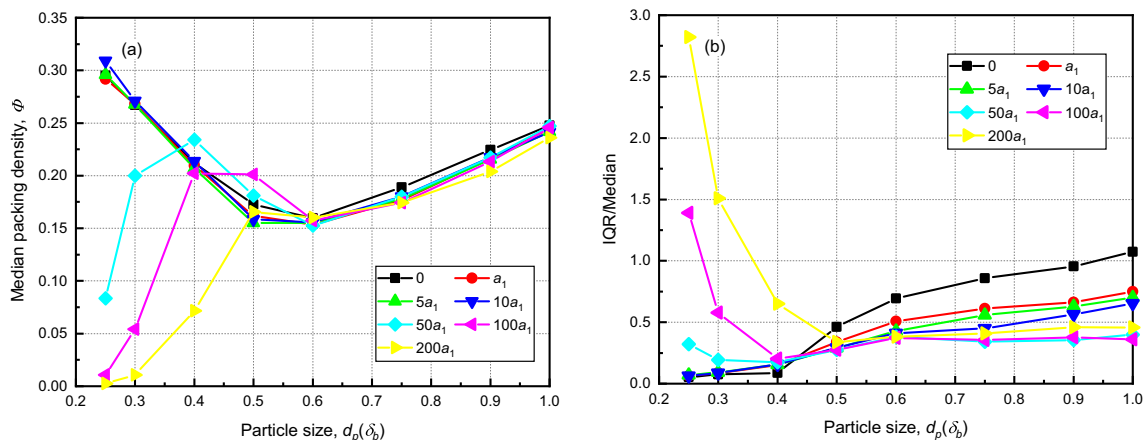

Fig. 9. Effect of particle size on (a) median packing density and (b) ratio IQR to median packing density for different Hamaker constants. The interquartile range (IQR) defines the range of the middle 50% of the ranked data.
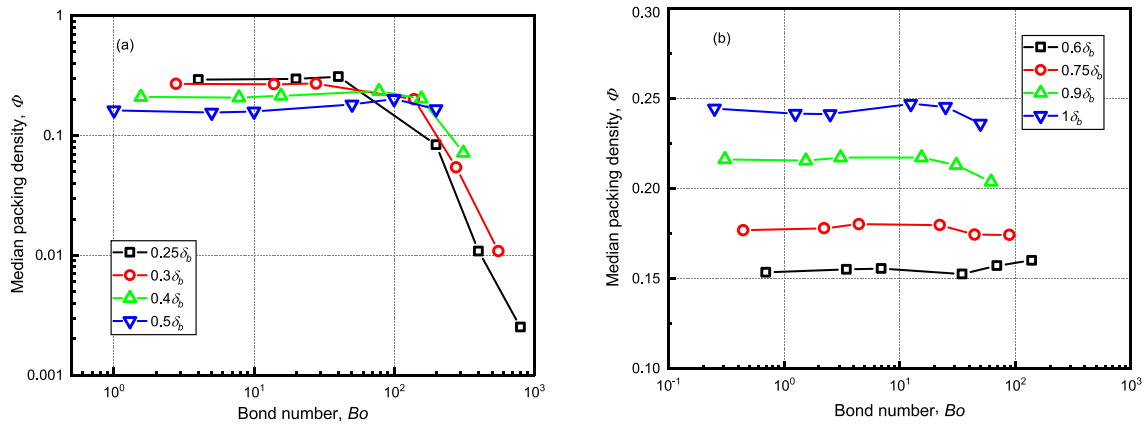
Fig. 10. Dependence of median packing density on *Bo* for (a) particles smaller than $0.5\delta_b$ and (b) particles larger than $0.5\delta_b$.
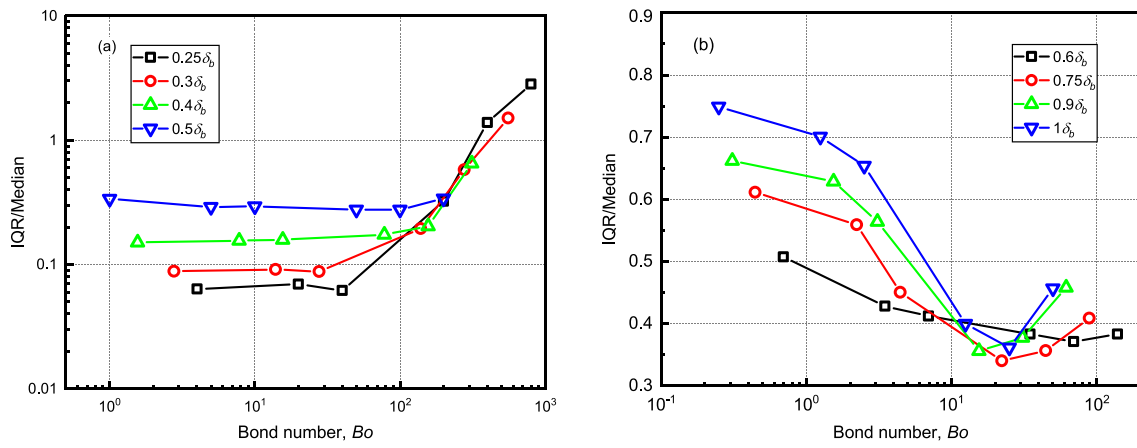

Fig. 11. Dependence of the IQR/median ratio on *Bo* for (a) small particles (i.e., $d_p/\delta_b \leq 0.5$) and (b) large particles (i.e., $d_p/\delta_b > 0.5$).
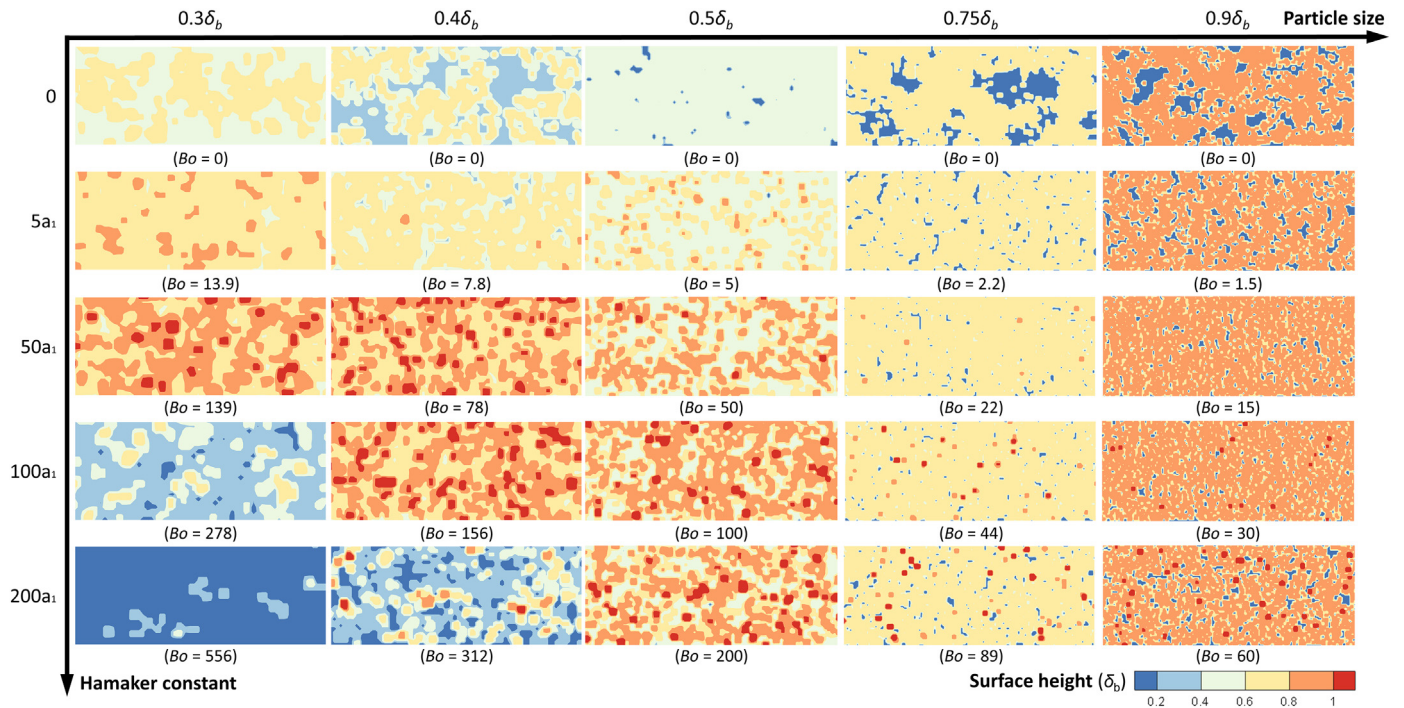

Fig. 12. Surface profile of spread powder layer for different particle sizes and Hamaker constants, where the surface height is normalized with blade clearance.
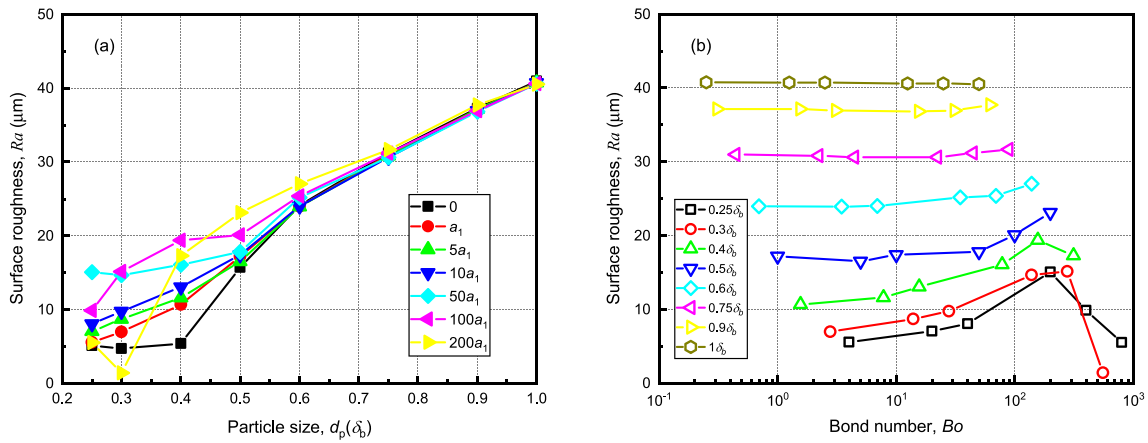
Fig. 13. Surface roughness of the spread powder layer as a function of (a) particle size and (b) Bond number.

present a better surface uniformity compared to that of cohesive particles, as most of the surface heights are found within a narrower range. It is worth noting that the turning point depends on particle size, for example, $50a_1$ for $0.25\delta_b$, $100a_1$ for $0.3\delta_b$ and $200a_1$ for $0.4\delta_b$. This is because, for a given Hamaker constant, the magnitude of van der Waals force relative to particle gravity is inversely proportional to the square of particle size, as per the definition of Bond number. In contrast, due to the dominant mono-layered structure of large particles (i.e., $d_p >$ $0.5\delta_b$), the ratio of primary surface height first increases and then decreases with Hamaker constant, with an optimal surface uniformity observed at $50a_1$ for cohesive particle of size $0.75\delta_b$ and $0.9\delta_b$.

Fig. 13(a) shows the surface roughness as a function of particle size for different Hamaker constants, which is calculated as the arithmetical mean deviation of surface height. Decreasing particle size leads to a nearly linear drop of the surface roughness before reaching a critical particle size of $0.5\delta_b$, corresponding to a structure transition from a mono-layered to a multiple-layered packing. This linear decline is largely preserved over particles with different Hamaker constants, although a slightly larger slope is observed for particles with a smaller Hamaker constant. For particles smaller than the $0.5\delta_b$, surface roughness remains relatively stable for non-cohesive particles, suggesting an optimum surface homogeneity due to particle rearrangement in multiple layered powder bed. In contrast, cohesive particles present a continuous drop in surface roughness with decreasing particle size, the extent of which depends on Hamaker constants. It is worth noting that the significant drop of the surface roughness for the strongly cohesive particles (i.e., $A \geq 100a_1$ and $d_p < 0.3\delta_b$) is due to the fact that particles get difficult

to be discharged from the blade, as van der Waals force dominates over particle gravity. Fig. 13(b) shows the surface roughness as a function of Bo. It can be seen that surface roughness is mainly determined by geometrical effect for particles larger than $0.5\delta_b$, as a result of the mono-layered packing structure. For particles smaller than $0.5\delta_b$, surface roughness increases with Bo up to 200. As explained before, the considerable drop of surface roughness for $Bo > 200$ is caused by the small number of particles being deposited.

5.4. Effect of blade clearance

The efficacy of using a larger blade clearance to improve layer quality is further demonstrated in this section. Here, the difference in interparticle cohesion is only due to the effect of surface cohesiveness while size effect is controlled by increasing blade clearance. Fig. 14 shows the spread powder bed formed by particles of size 75 μm and 40 μm, respectively, with three different clearances examined: 100 μm, 150 μm and 200 μm. For a particle size of 75 μm, the change of blade clearance corresponds to a structure transition from a mono-layered packing to a multiple-layered packing, which results in a much denser powder layer. The layer homogeneity is also seen to increase, especially for a small Hamaker constant (i.e., $A < 50a_1$). For particle size of 40 μm, the spread powder bed is dominated by a multiple-layered structure. The increase of blade clearance results in a much denser and more uniform packing for particles with a small Hamaker constant (i.e., $A \leq 50a_1$) while shows little impact on layer quality for particles with a large Hamaker constant (i.e., $A > 50a_1$).
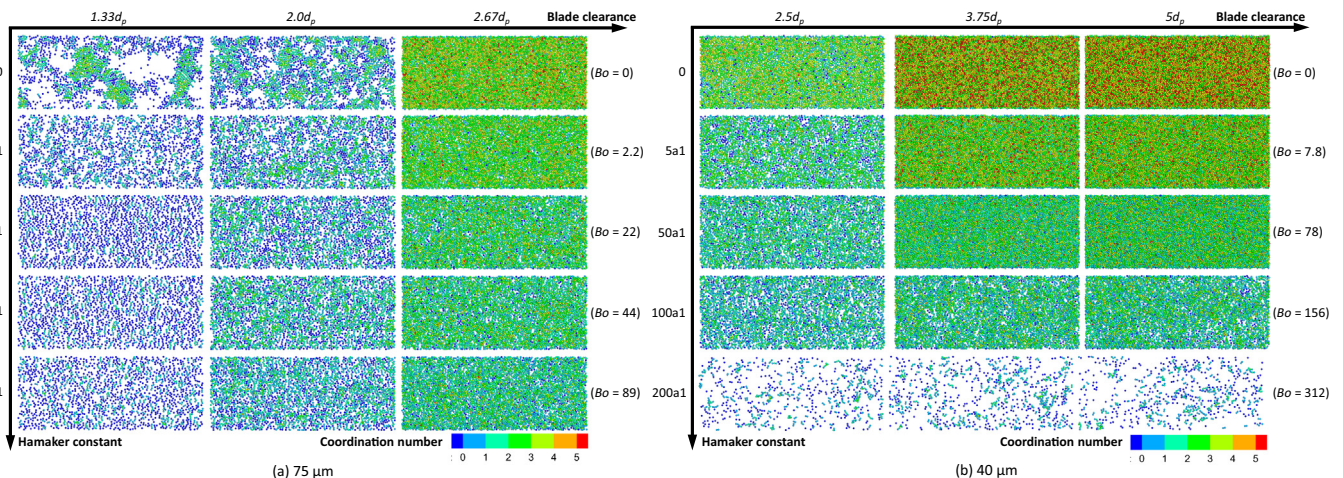

Fig. 14. Top view of spread powder bed for particle size of (a) 75 μm and (b) 40 μm. Only a section of the spread bed is shown here, with a dimension of 40dp × 100dp.
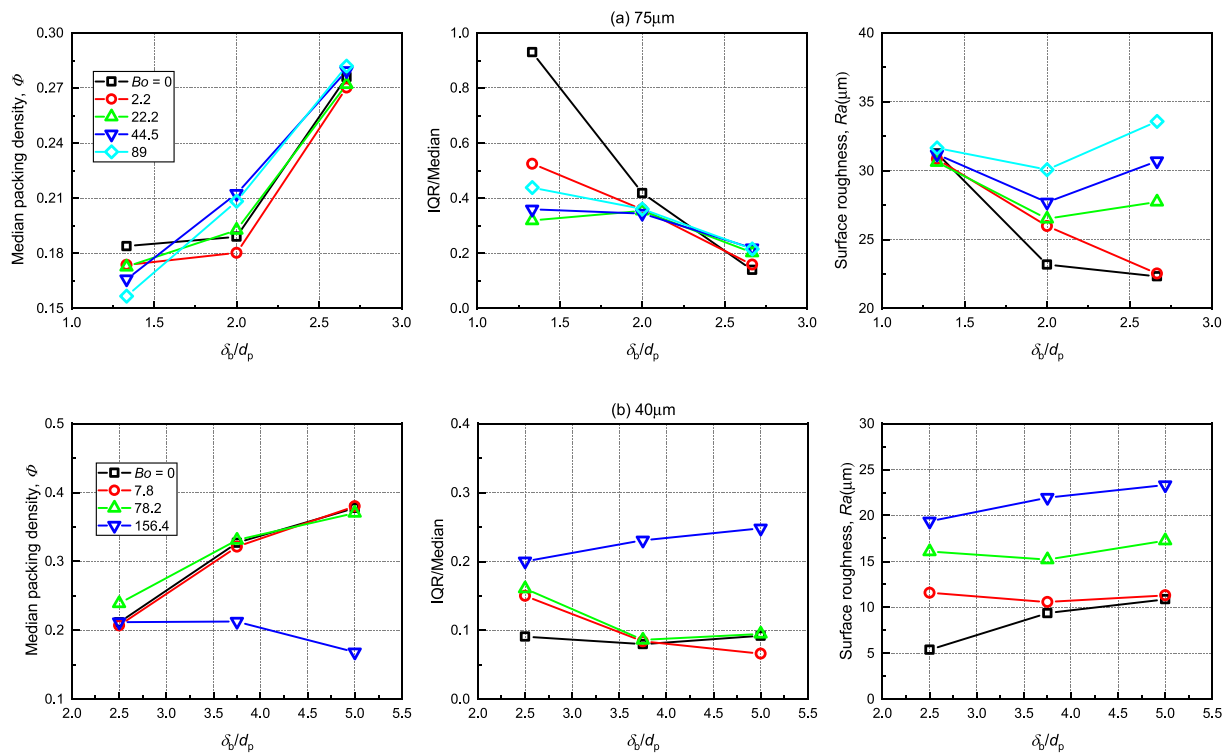
Fig. 15. Median packing density, ratio of IQR to median density and surface roughness for particle size of (a) 75 μm and (b) 40 μm.

Fig. 15 shows the quantitative change of median packing density, IQR/Median ratio, and surface roughness due to the increase of blade clearance. As shown in Fig. 15(a), for a particle size of 75 μm, particles with a small Bo (i.e., $Bo \leq 22.2$) present a significant increase in the median packing density when a multiple layered packing structure is allowed (i.e., from $\delta_b/d_p < 2$ to $\delta_b/d_p > 2$), which also suggests a higher efficiency of material deposition while a nearly linear dependence is observed at larger Bo (i.e., > 44). The layer homogeneity continues to improve and the difference due to particle cohesion diminishes with increasing blade clearance. However, surface roughness shows a contrary dependence on blade clearance, where the difference due to particle cohesion enlarges at a larger blade clearance. Particles with stronger cohesion shows a larger surface roughness at large blade clearance, possibly due to a large extent of particle agglomeration. For particles of size 40 μm, the rate of density increase decrease with increasing blade clearance. And little difference in the median packing density is observed over different Bo when it is smaller than 100. Both the homogeneity of packing density distribution and surface roughness show little variation with blade clearance when $\delta_b/d_p > 3.5$, indicating a reduced influence due to boundary effect.

6. Conclusions

In the present study, particle-scale simulations were conducted to address the combined effect of particle size and surface cohesiveness on the spreadability of cohesive fine powders for additive manufacturing. The present DEM model allows the van der Waals interactions to be explicitly considered and simulations to be accelerated by means of particle stiffness scaling and GPU computing. The DEM model was validated against literature data on static angle of repose formed by discharging Ti-6Al-4V powders from a vibrating funnel. With calibrated effective surface energy, the predicted angle of repose shows good agreement with experiments for samples of different particle size distributions. On this basis, particle size and surface cohesiveness were systematically varied, with their combined effects examined at both macroscopic and microscopic levels. The main conclusions are summarised as follows,

- A better layer quality can be obtained either by small particles with weak surface cohesiveness or large particles with moderate surface cohesiveness, whilst strong surface cohesiveness leads to a sparse and non-uniform spread powder layer.
- The frequency distribution of CN largely follows a Gaussian distribution for small particles of weak surface cohesiveness, which shifts towards left and gets truncated at the lower side with the increase of either particle size or surface cohesiveness. For particles of large size or strong cohesiveness, CN decays exponentially due to strong wall effect.
- The median packing density first decreases and then increases with decreasing particle size, except a sharp drop observed at small particles with strong surface cohesiveness. Decreasing particle size can improve density homogeneity for weakly cohesive particles but not for strongly cohesive particles.
- Surface roughness of spread layer declines with decreasing particle size, with a larger degree of decrease observed for particles with a smaller surface cohesiveness.
- The layer quality is controlled by two competing effects: geometrical effect due to the constraint of blade clearance (d_p/δ_b) and cohesive effect due to interparticle cohesion (Bo). The cohesive effect takes over geometrical effect as the dominant factor governing particle deposition in spreading when $Bo > 100$.
- The efficacy of increasing blade clearance to improve layer quality is affected by both interparticle cohesion and the relative size between particle and blade clearance, not showing a positive effect on all metrics.

The mechanisms underlying spreading depends on both particle size and surface cohesiveness. For weakly cohesive powders, particles possess a high level of residual momentum after being discharged from the blade. A dense and uniform packing can be obtained for small particles because of an enhanced particle rearrangement while the spread layer of large particles features a mono-layered, non-uniform packing structure due to collision-induced energy dissipation. When multiple-layered packing structure is allowed, the increase of surface cohesiveness can promote particle agglomeration, showing a decrease in the

surface homogeneity of the spread powder layer. For strongly cohesive powders, the strong interparticle attractive forces hinder the discharge of small particles from the blade, leading to a sparse and non-uniform structure while it promotes the form of chain-like agglomerates for larger particles, leading to localized regions of high packing density.

The present study highlights the interplay between geometrical effect and particle cohesion. Surface modification of particles is more effective to increase layer homogeneity for larg e particles while mean packing density is controlled more by the relative size between particle and blade gap. Since both layer homogeneity and mean packing density are critical for powder spreading, understanding the combined effect of particle size and surface cohesiveness can help identify the most cost-effective approach to improve the quality of a spread layer. However, it is worthwhile to note that the dispersity of particle properties, such as size, shape, density, and surface cohesiveness, further complicates the dominant mechanism for spreading. This requires further extensive investigation and will be addressed in the future work.

Declaration of Competing Interest

The authors declare that they have no known competing financial interests or personal relationships that could have appeared to influence the work reported in this paper.

Acknowledgments

References

[1] U. Ali, Y. Mahmoodkhani, S. Imani Shahabad, R. Esmaeilizadeh, F. Liravi, E. Sheydaeian, K.Y. Huang, E. Marzbanrad, M. Vlasea, E. Toyserkani, On the measurement of relative powder-bed compaction density in powder-bed additive manufacturing processes, Mater. Des. 155 (2018) 495–501, https://doi.org/10.1016/j.matdes.2018.06.030.

[2] J.H. Tan, W.L.E. Wong, K.W. Dalgarno, An overview of powder granulometry on feedstock and part performance in the selective laser melting process, Addit. Manuf. 18 (2017) 228–255, https://doi.org/10.1016/j.addma.2017.10.011.

[3] R.Y. Yang, R.P. Zou, A.B. Yu, Computer simulation of the packing of fine particles, Phys. Rev. E 62 (2000) 3900–3908, https://doi.org/10.1103/PhysRevE.62.3900.

[4] C. Meier, R. Weissbach, J. Weinberg, W.A. Wall, A. John Hart, Modeling and characterization of cohesion in fine metal powders with a focus on additive manufacturing process simulations, Powder Technol. 343 (2019) 855–866, https://doi.org/10.1016/j.powtec.2018.11.072.

[5] S.E. Brika, M. Letenneur, C.A. Dion, V. Brailovski, Influence of particle morphology and size distribution on the powder flowability and laser powder bed fusion manufacturability of Ti-6Al-4V alloy, Addit. Manuf. 31 (2020) 100929, https://doi.org/10.1016/j.addma.2019.100929.

[6] M.A. Balbaa, A. Ghasemi, E. Fereiduni, M.A. Elbestawi, S.D. Jadhav, J.-P. Kruth, Role of powder particle size on laser powder bed fusion processability of AlSi10Mg alloy, Addit. Manuf. (2020), 101630 https://doi.org/10.1016/j.addma.2020.101630.

[7] S. Touzé, M. Rauch, J.Y. Hascoët, Flowability characterization and enhancement of aluminium powders for additive manufacturing, Addit. Manuf. 36 (2020) 101462, https://doi.org/10.1016/j.addma.2020.101462.

[8] S. Haeri, S. Haeri, J. Hanson, S. Lotfian, Analysis of radiation pressure and aerodynamic forces acting on powder grains in powder-based additive manufacturing, Powder Technol. 368 (2020) 125–129, https://doi.org/10.1016/j.powtec.2020.04.031.

[9] A.B. Spierings, N. Herres, G. Levy, Influence of the particle size distribution on surface quality and mechanical properties in AM steel parts, Rapid Prototyp. J. 17 (2011) 195–202, https://doi.org/10.3929/ethz-a-010782581.

[10] K. Riener, N. Albrecht, S. Ziegelmeier, R. Ramakrishnan, L. Haferkamp, A.B. Spierings, G.J. Leichtfried, Influence of particle size distribution and morphology on the

[11] L.I. Escano, N.D. Parab, L. Xiong, Q. Guo, C. Zhao, K. Fezzaa, W. Everhart, T. Sun, L. Chen, Revealing particle-scale powder spreading dynamics in powder-bed-based additive manufacturing process by high-speed x-ray imaging, Sci. Rep. 8 (2018) 1–11, https://doi.org/10.1038/s41598-018-33376-0.

[12] K.J. Dong, R.Y. Yang, R.P. Zou, A.B. Yu, Role of interparticle forces in the formation of random loose packing, Phys. Rev. Lett. 96 (2006) 1–4, https://doi.org/10.1103/PhysRevLett.96.145505.

[13] M. Halidan, G.R. Chandratilleke, K. Dong, A. Yu, The effect of interparticle cohesion on powder mixing in a ribbon mixer, AICHE J. 62 (2016) 1023–1037, https://doi.org/10.1002/aic.15101.

[14] M. Capece, K.R. Silva, D. Sunkara, J. Strong, P. Gao, On the relationship of interparticle cohesiveness and bulk powder behavior: Flowability of pharmaceutical powders, Int. J. Pharm. 511 (2016) 178–189, https://doi.org/10.1016/j.ijpharm.2016.06.059.

[15] S. Haeri, Y. Wang, O. Ghita, J. Sun, Discrete element simulation and experimental study of powder spreading process in additive manufacturing, Powder Technol. 306 (2017) 45–54, https://doi.org/10.1016/j.powtec.2016.11.002.

[16] W. Nan, M. Pasha, T. Bonakdar, A. Lopez, U. Zafar, S. Nadimi, M. Ghadiri, Jamming during particle spreading in additive manufacturing, Powder Technol. 338 (2018) 253–262, https://doi.org/10.1016/j.powtec.2018.07.030.

[17] Y.M. Fouda, A.E. Bayly, A DEM study of powder spreading in additive layer manufacturing, Granul. Matter 22 (2020) 1–18, https://doi.org/10.1007/s10035-019-0971-x.

[18] S. Haeri, Optimisation of blade type spreaders for powder bed preparation in additive manufacturing using DEM simulations, Powder Technol. 321 (2017) 94–104, https://doi.org/10.1016/j.powtec.2017.08.011.

[19] H. Chen, Q. Wei, S. Wen, Z. Li, Y. Shi, Flow behavior of powder particles in layering process of selective laser melting: numerical modeling and experimental verification based on discrete element method, Int. J. Mach. Tools Manuf. 123 (2017) 146–159, https://doi.org/10.1016/j.ijmachtools.2017.08.004.

[20] C. Meier, R. Weissbach, J. Weinberg, W.A. Wall, A.J. Hart, Critical influences of particle size and adhesion on the powder layer uniformity in metal additive manufacturing, J. Mater. Process. Technol. 266 (2019) 484–501, https://doi.org/10.1016/j.jmatprotec.2018.10.037.

[21] L. Wang, E.L. Li, H. Shen, R.P. Zou, A.B. Yu, Z.Y. Zhou, Adhesion effects on spreading of metal powders in selective laser melting, Powder Technol. 363 (2020) 602–610, https://doi.org/10.1016/j.powtec.2019.12.048.

[22] Y. Ma, T.M. Evans, N. Philips, N. Cunningham, Numerical simulation of the effect of fine fraction on the flowability of powders in additive manufacturing, Powder Technol. 360 (2020) 608–621, https://doi.org/10.1016/j.powtec.2019.10.041.

[23] D. Yao, X. An, H. Fu, H. Zhang, X. Yang, Q. Zou, K. Dong, Dynamic investigation on the powder spreading during selective laser melting additive manufacturing, Addit. Manuf. 37 (2020), 101707 https://doi.org/10.1016/j.addma.2020.101707.

[24] M.Y. Shaheen, A.R. Thornton, S. Luding, T. Weinhart, The influence of material and process parameters on powder spreading in additive manufacturing, Powder Technol. 383 (2021) 564–583, https://doi.org/10.1016/j.powtec.2021.01.058.

[25] Y. He, A. Hassanpour, A.E. Bayly, Linking particle properties to layer characteristics: discrete element modelling of cohesive fine powder spreading in additive manufacturing, Addit. Manuf. (2020), 101685 https://doi.org/10.1016/j.addma.2020.101685.

[26] Y. He, A. Hassanpour, M.A. Behjani, A.E. Bayly, A novel stiffness scaling methodology for discrete element modelling of cohesive fine powders, Appl. Math. Model. 90 (2021) 817–844, https://doi.org/10.1016/j.apm.2020.08.062.

[27] R.D. Mindlin, H. Deresiewicz, Elastic spheres in contact under varying oblique forces, ASME - J. Appl. Mech. 20 (1953) 327–344.

[28] H.C. Hamaker, The London-van der Waals attraction between spherical particles, Physica. 4 (1937) 1058–1072, https://doi.org/10.1016/S0031-8914(37)80203-7.

[29] K.L. Johnson, K. Kendall, A.D. Roberts, Surface energy and the contact of elastic solids, Proc. R. Soc. Lond. A. Math. Phys. Sci. 324 (1971) 301–313, https://doi.org/10.1098/rspa.1971.0141.

[30] S. Li, J.S. Marshall, G. Liu, Q. Yao, Adhesive particulate flow: the discrete-element method and its application in energy and environmental engineering, Prog. Energy Combust. Sci. 37 (2011) 633–668, https://doi.org/10.1016/j.pecs.2011.02.001.

[31] S. Roy, A. Singh, S. Luding, T. Weinhart, Micro–macro transition and simplified contact models for wet granular materials, Comput. Part. Mech. 3 (2016) 449–462, https://doi.org/10.1007/s40571-015-0061-8.

[32] E.J.R. Parteli, J. Schmidt, C. Blümel, K.E. Wirth, W. Peukert, T. Pöschel, Attractive particle interaction forces and packing density of fine glass powders, Sci. Rep. 4 (2014) 6227, https://doi.org/10.1038/srep06227.

[33] Y. He, J. Gardy, A. Hassanpour, A.E. Bayly, A digital-based approach for characterising spread powder layer in additive manufacturing, Mater. Des. (2020), 109102 https://doi.org/10.1016/j.matdes.2020.109102.